Quasi-parallel Antisunward-propagating Whistler Waves Associated with the Electron Deficit in the Near-Sun Solar Wind: Particle-in-cell Simulation

Alfredo Micera[1] , Daniel Verscharen[2] , Jesse T. Coburn[2,3] , and Maria Elena Innocenti[1]

[1] Institut für Theoretische Physik, Ruhr-Universität Bochum, Bochum, Germany; alfredo.micera@rub.de
[2] Mullard Space Science Laboratory, University College London, Dorking, UK
[3] Space Science Institute, Boulder, CO 80301, USA

Abstract

In situ observations of the solar wind have shown that the electron velocity distribution function (VDF) consists of a quasi-Maxwellian core, comprising most of the electron population, and two sparser components: the halo, which are suprathermal and quasi-isotropic electrons, and an escaping beam population, the strahl. Recent Parker Solar Probe (PSP) and Solar Orbiter (SO) observations have added one more ingredient to the known nonthermal features, the deficit—a depletion in the sunward region of the VDF, already predicted by exospheric models but never so extensively observed. By employing particle-in-cell simulations, we study electron VDFs that reproduce those typically observed in the inner heliosphere and investigate whether the electron deficit may contribute to the onset of kinetic instabilities. Previous studies and in situ observations show that strahl electrons drive oblique whistler waves unstable, which in turn scatters them. As a result, suprathermal electrons can occupy regions of phase space where they fulfill resonance conditions with the parallel-propagating whistler wave. The suprathermal electrons lose kinetic energy, resulting in the generation of unstable waves. The sunward side of the VDF, initially depleted of electrons, is gradually filled, as this wave−particle interaction process, triggered by the depletion itself, takes place. Our findings are compared and validated against current PSP and SO observations: among others, our study provides a mechanism explaining the presence in the heliosphere of regularly observed parallel antisunward whistler waves, suggests why these waves are frequently observed concomitant with distributions presenting an electron deficit, and describes a noncollisional heat flux regulating process.

Unified Astronomy Thesaurus concepts: Plasma astrophysics (1261); Solar wind (1534); Space plasmas (1544)

Materials only available in the online version of record: animations

1. Introduction

The Parker Solar Probe (PSP; N. J. Fox et al. 2016) and Solar Orbiter (SO; D. Müller et al. 2013) missions have provided valuable evidence confirming the fundamental role of electrons in coronal and solar wind dynamics. Electrons are lighter than ions: their thermal velocity at the corona is large enough for many of them to escape the Sun's gravity. An ambipolar electric field is then established, which decelerates electrons and accelerates protons, so as to maintain equal electron and ion fluxes in the radial direction (N. Meyer-Vernet 2007). The existence of this ambipolar field has been predicted and explained in the context of exospheric models (K. Jockers 1970; J. Lemaire & M. Scherer 1971; M. Maksimovic et al. 2001; I. Zouganelis et al. 2005), which assume collisionless particle dynamics above a reference level called the exobase. It has also been studied in global-scale models, where increased levels of collisionality are used as a proxy for wave/particle interaction (Ø. Lie-Svendsen et al. 1997; V. Pierrard et al. 1999; S. Landi & F. Pantellini 2003).

The ambipolar electric field deeply influences electron circulation patterns in interplanetary space and hence the shape of the electron VDFs. Three electron populations are present in the solar wind: escaping, trapped, and ballistic electrons. Escaping electrons have energy larger than the asymptotic ambipolar potential energy and stream away to increasingly larger radial distances. Both ballistic and trapped electrons are turned back toward the Sun by the ambipolar electric potential. Ballistic electrons are the ones that "fall back" into the collisional coronal reservoir. Trapped electrons are the ones that are again turned back, this time toward increasing radial distance, by the mirror force in the sunward-increasing magnetic field (J. Lemaire & M. Scherer 1973; V. Pierrard & J. Lemaire 1996; J. D. Scudder 1996; M. Maksimovic et al. 1997; N. Meyer-Vernet & K. Issautier 1998; S. Landi & F. Pantellini 2003; I. Zouganelis et al. 2005; S. Boldyrev et al. 2020).

The typical electron VDF observed in the solar wind, composed of three electron populations (core, strahl, and halo; W. C. Feldman et al. 1975; H. Rosenbauer et al. 1977; W. G. Pilipp et al. 1987; M. Maksimovic et al. 2005; V. Stverák et al. 2009; J. S. Halekas et al. 2020), is a direct consequence of this large-scale process. Ballistic and trapped electrons form the core, while escaping electrons constitute the strahl. Scattered strahl electrons give rise to the halo (e.g., V. Stverák et al. 2009). Strahl-to-halo scattering has been observed in a number of kinetic models (C. Vocks et al. 2005; S.-Y. Jeong et al. 2020; B. Tang et al. 2020), including fully kinetic particle-in-cell simulations (A. Micera et al. 2020b, 2021). It is also indirectly confirmed by the anticorrelation between the fractional density of the strahl and halo populations observed, e.g., in M. Maksimovic et al. (2005) and V. Stverák et al. (2009) at $r > 0.3$ au, where r is the heliocentric distance, and more recently by J. S. Halekas et al. (2020) and L. Berčič et al. (2020) in PSP data. Interestingly, one can find

an early, indirect observation of strahl-to-halo scattering in E. E. Scime et al. ([1994](#)). There, the radial heat flux evolution in Ulysses data (1 au $< r <$ 5 au) is compared with expectations from collisionless expansion of a suprathermal population (called there a "halo") along magnetic field lines. The observed heat flux exhibits a $\propto r^{-3}$ radial dependence, decreasing more sharply than the sole effect of expansion. This is compatible with a scenario where the heat-flux-carrying strahl reduces faster than what is expected from expansion alone, as a result of strahl-to-halo scattering processes. A radial evolution of strahl density faster than the so-called "spiral" expansion (more appropriate for the strahl population than "radial" expansion, following the terminology in V. Stverák et al. [2009](#)) is directly observed by V. Stverák et al. ([2009](#)).

In A. Micera et al. ([2021](#)), fully kinetic expanding-box simulations run with the semi-implicit EB-iPic3D code (M. E. Innocenti et al. [2019](#), [2020](#)) demonstrate halo formation from scattering of strahl electrons owing to the oblique whistler heat flux instability. The simulation is initialized with a (stable) electron VDF and plasma parameters that accurately reproduce those measured during PSP Encounter I. Radial expansion self-consistently drives the solar wind in a regime where it is unstable with respect to whistler heat flux instability. C. Cattell et al. ([2021](#)) provide strong observational evidence for this numerically predicted scenario: the direct evidence for pitch-angle scattering of strahl electrons by narrowband whistler-mode waves in PSP observations.

The presence of the ambipolar electric potential in interplanetary space leaves a distinct signature in the electron VDFs, namely the so-called electron deficit in the sunward magnetic-field-aligned direction. The "missing" returning electrons are those energetic enough to escape the electrostatic potential. Early deficit observations in Helios data down to $65R_s$ (W. G. Pilipp et al. [1987](#)) have been recently corroborated by PSP (J. S. Halekas et al. [2020](#); L. Berčič et al. [2021a](#); J. S. Halekas et al. [2021a](#)) and SO observations (L. Berčič et al. [2021b](#); J. T. Coburn et al. [2024](#)). In L. Berčič et al. ([2021a](#)), a number of VDF measurements collected between $20.3R_s$ and $85.3R_s$, with R_s the solar radius, during PSP Encounters 4−7 are used to calculate the location in energy of the deficit ("cutoff energy") and, from that, the ambipolar potential between a specific location and its asymptotic value. They measure a radial dependence of $r^{-0.66}$. In J. S. Halekas et al. ([2021a](#)), the statistical properties of the deficit are highlighted. The deficit is observed more frequently closer to the Sun (below 0.2 au the deficit occurs in 60%–80% of observations, while clear signs of its presence appear less frequently at larger distances), with lower fractional halo density, smaller electron parallel beta, lower collisional age, and more anisotropic core distributions. This suggests causality or correlation between the processes that isotropize electron VDFs (e.g., strahl-to-halo electron scattering) and those that erase deficit signatures. J. S. Halekas et al. ([2021a](#)) suggest two possible mechanisms for deficit erasure by collisionless processes. One possibility is a multistep process, similar to the one proposed by A. Micera et al. ([2020b](#), [2021](#)), which scatters strahl electrons into the halo and then relaxes into parallel whistler waves. These waves would further isotropize the distribution by scattering halo electrons at all pitch angles, thus erasing the deficit. A second possibility is an instability triggered by an unstable deficit, as suggested by L. Berčič et al. ([2021b](#)) and further explored by J. T. Coburn et al. ([2024](#)). There, quasi-parallel right-hand polarized whistler waves are observed in SO field data at $112R_s$, in the presence of the electron deficit. Resonance condition

analysis supports the hypothesis of an antisunward, quasi-parallel whistler instability driven by electrons scattering from higher to lower energies. Such an instability would contribute to erase the electron deficit.

In A. Micera et al. ([2020b](#)) it has not been ascertained whether the parallel whistler waves that scatter nascent halo electrons at the highest pitch angles are a result of the relaxation of the oblique whistler heat flux instability. Alternatively, these parallel whistler waves might form independently, triggered by changes in the electron VDF, as suggested in L. Berčič et al. ([2021b](#)). In addition, in A. Micera et al. ([2021](#)) most of the parallel whistler waves are sunward directed, being essentially formed from the relaxation of the whistler heat flux instability triggered by the strahl. However, the waves that resonantly scatter the sunward deficit can only propagate antisunward (L. Berčič et al. [2021b](#)).

In this work, we simulate via fully kinetic particle-in-cell simulation a VDF resembling that obtained in A. Micera et al. ([2020a](#), [2021](#)), to elucidate the relation between strahl-to-halo scattering, quasi-parallel whistler waves, and electron deficit erasure. To do so, we initialize our simulation with a configuration that is not unstable to the whistler heat flux instability to isolate instabilities directly driven by the electron deficit, if they occur at all.

This paper is organized as follows: In Section [2](#), we show the simulation setup and describe in detail our initial conditions, motivating them in the context of solar wind electron dynamics. In Section [3](#), we show the results of the simulation by analyzing waves, particle distributions, and their mutual interactions. Finally, in Section [4](#), we discuss our results, compare and validate them against recent observations conducted by PSP and SO, and draw our conclusions.

2. Setup of the PIC Simulation

We perform a 2D PIC simulation with iPic3D (S. Markidis et al. [2010](#); M. E. Innocenti et al. [2017](#)), a fully kinetic code that uses a semi-implicit scheme (G. Lapenta et al. [2006](#)) to couple the Maxwell equations governing electromagnetic fields and the equations of motion that describe the dynamics of particles. Thanks to the semi-implicit approach, small temporal and spatial scales can be retained, without the requirement to resolve the Debye length and the inverse electron plasma frequency as is the case in explicit codes (R. W. Hockney & J. W. Eastwood [1988](#)) and thus including electronic scales and at the same time employing a domain of the order of several ion skin depths.

We model a noncollisional plasma, consisting of electrons and protons, embedded in an initially uniform magnetic field. The initial background magnetic field is of magnitude 0.00045 G and is directed along the x-direction ($B_0 = B_0 \ \hat{e}_x$), which is the direction we denote as parallel ($\parallel$). Positive x is the antisunward direction. Here y and z are the two perpendicular directions that we denote as $\perp_1$ and $\perp_2$, respectively.

The units used for normalization are as follows: for velocities, the speed of light c; for lengths, the proton skin depth $d_p = c/\omega_p$; and for the time, the inverse of the proton plasma frequency $\omega_p = \sqrt{4\pi e^2 n_p/m_p}$, with n_p the proton number density, m_p the proton mass, and e the elementary charge.

The computational domain consists of a 2D box of size $L_{x,y} = 8d_p$, discretized with 512^2 grid points so that the spatial resolution is $\Delta_{x,y} = d_p/64$. The time step used is $0.05\omega_p^{-1}$. We use a realistic proton-to-electron mass ratio ($\mu = m_p/m_e = 1836$) and 1024 protons and 4096 electrons per cell. The choice of such
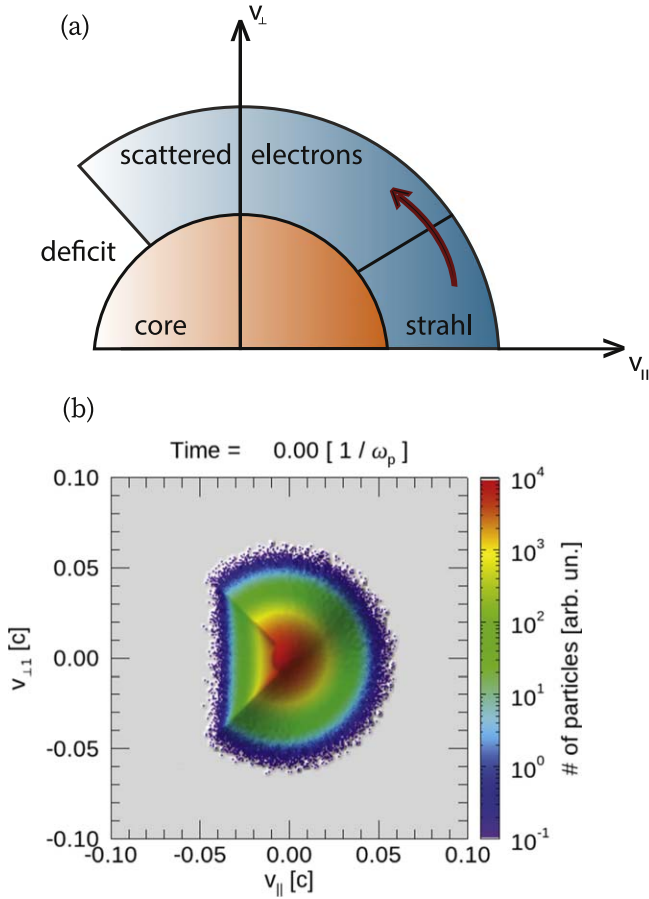
Figure 1. (a) Schematic example of the electron distribution function used to initialize the simulation. The orange area denotes the region of the phase space that can be occupied by trapped and ballistic electrons, while the blue area denotes the region that can be occupied by escaping and scattered electrons. (b) Electron VDF $f_e = f(v_{\parallel}, v_{\perp 1})$ at $t_0 = 0$. The phase space is integrated over $v_{\perp 2}$.

a setup results from convergence tests conducted to find a resolution and number of particles such that the energy is conserved almost perfectly and to have satisfactory statistics for the region of phase space occupied by suprathermal electrons.

The initial electron distribution consists of an electron core (in orange in the sketch image in Figure 1(a)), plus suprathermal electrons (strahl + nascent halo, depicted in blue). Here the suprathermal electrons are the sum of escaping electrons (the strahl) plus those that are scattered during the interaction between the strahl and oblique whistler waves and thus acquire higher perpendicular velocities (A. Micera et al. 2020b; C. Cattell et al. 2021; A. Micera et al. 2021). The scattered electrons can populate the suprathermal trajectories around and up to above $90°$ pitch angle and can be seen as incipient halo electrons. Underlying our initial condition is the process whereby in a deficit−strahl system, due to the generation of oblique whistler waves, electrons with high $v_{\perp}$ and $v_{\parallel} \leqslant 0$ can be obtained. This process has already been simulated in the framework of the solar wind in A. Micera et al. (2020b, 2021) and in other applications in which the electron distribution function is modeled through the employment of PIC simulations (e.g., S. Komarov et al. 2018; G. T. Roberg-Clark et al. 2019). Here we start from the scenario where part of the strahl electrons have already been scattered and the halo is not fully formed, and thus the sunward deficit is not fully filled by the suprathermal electrons. This is a configuration

that can be commonly observed at certain heliocentric distances where the three typical suprathermal features of the electron VDF can coexist: the strahl, a tenuous halo, and the deficit (e.g., L. Berčič et al. 2021a; J. S. Halekas et al. 2021a).

The choice of employing such an electron distribution function, which is the product of a transient regime, to initialize our simulations derives from the interest in understanding the interplay between the various suprathermal components of the electron VDF: in particular, whether the wave−particle interactions that lead to the formation of the halo at the expense of the strahl also have an effect in filling the deficit as the solar wind travels through interplanetary space.

For these reasons, the initial electron VDF consists of a drifting Maxwellian, from which we cut a solid angle in the sunward region of the phase space: the "missing" electrons model the electron deficit. The drifting Maxwellian is defined as follows:

$$
\begin{aligned}
f_e(v_{\parallel}, v_{\perp}, t = 0) \\
= \frac{(2\pi)^{-3/2}}{w_{\perp e}^2 w_{\parallel e}} \exp\left(-\frac{v_{\perp}^2}{2w_{\perp e}^2} - \frac{(v_{\parallel} - u_e)^2}{2w_{\parallel e}^2}\right),
\end{aligned} \tag{1}
$$

with $w_e = \sqrt{k_B T_e / m_e}$ the electron thermal velocity, k_B the Boltzmann constant, and T_e the electron temperature. The deficit in the electron VDF (of which we observe a 2D projection in Figure 1(b) is modeled by excluding from the distribution the electrons whose velocities satisfy the following quadratic law:

$$
v_{\parallel} < -p \quad \sqrt{(v_{\perp 1}^2 + v_{\perp 2}^2)}. \tag{2}
$$

The parameter p represents the free parameter through which we decide the angle at which to cut our VDF in the plane. Thus, in this paper, we have chosen to use $p = 1$ to obtain a cut between the angles $\alpha = 90° + \arctan(\sqrt{(v_{\perp 1}^2 + v_{\perp 2}^2)}/v_{\parallel}) = 144°$ and $\alpha_1 = 360° - \alpha = 216°$.

Protons are assumed to be initially isotropic and Maxwellian. The proton and electron temperatures are chosen so that $\beta_p = 1.7$ and $\beta_{e\parallel} = 1.5$, where $\beta_{j\parallel} = 8\pi n_j k_B T_{j\parallel}/B_0^2$ and subscript j denotes the species (p, e). We assume that their drift velocity is zero ($u_i = 0$). To ensure that the zero net current condition is satisfied, we impose a sunward drift on the electron distribution ($u_e = -0.004c$), which balances the current due to the initial VDF choice. This adjustment is crucial to maintain zero net current. Indeed, the absence of electrons associated with the electron deficit in the sunward direction would result in an antisunward-directed drift speed if the peak of the Maxwellian were centered at $v_{\parallel}/c = 0$. To ensure that the net plasma current at initialization is zero, we added a negative drift to the electron distribution so that the total electron current at initialization is zero. Additionally, the plasma is required to satisfy the quasi-neutrality condition ($n_p = n_e$), and we ensure that the proton and electron densities are equal.

3. Simulation Results

We let the plasma evolve from its initial condition, described in Section 2, and measure the energy exchanges within the simulated system. Figure 2 shows the temporal evolution of the variation of magnetic energy, kinetic energy, and total energy (electromagnetic energy plus kinetic energy) in the simulation. All energy variations shown in Figure 2 are offset by their initial values and normalized with respect to the total energy of

the system at the initialization:

$$\Delta\epsilon / \epsilon_{\text{tot},0} = (\epsilon - \epsilon_0)/\epsilon_{\text{tot},0}. \quad (3)$$

The blue curve represents the evolution over time of the normalized magnetic energy variation, with magnetic energy evaluated as

$$\epsilon_B = \frac{1}{8\pi} \int_V (B_x^2 + B_y^2 + B_z^2) \; dV. \quad (4)$$

The magnetic energy, after an initial phase in which it remains constant, presents an exponential growth starting at about $t = 50\omega_p^{-1}$. The magnetic energy reaches a peak at time $72\omega_p^{-1}$, after which it smoothly decreases until the end of the simulation. The curve in red, i.e., the normalized variation of the kinetic energy of the plasma ($\Delta\epsilon_K/\epsilon_{\text{tot},0}$) with kinetic energy evaluated as

$$\epsilon_K = \frac{1}{2}m_e v_e \cdot v_e + \frac{1}{2}m_p v_i \cdot v_i, \quad (5)$$

is antisymmetric to the curve representing the magnetic energy variation over time. This is due to an interchange of kinetic and magnetic energies in the simulated system (the energy gained by the magnetic field is lost by the particles and vice versa). After an initial quasi-stationary phase, an electromagnetic instability is triggered, which leads to a process of wave amplification at the expense of the kinetic energy of the electrons. Due to their initial configuration, the electrons have free energy that is gradually transferred to the electromagnetic fields during the growth phase of the instability. Once the magnetic energy has peaked, we enter the saturation phase of the instability, where the magnetic energy is converted back into kinetic energy. In Figure 2, the black curve represents the relative change of the total energy with respect to its value at initialization ($\Delta\epsilon_{\text{tot}}/\epsilon_{\text{tot},0}$) with

$$\epsilon_{\text{tot}} = \epsilon_B + \epsilon_K + \epsilon_E \quad (6)$$

and

$$\epsilon_E = \frac{1}{8\pi} \int_V (E_x^2 + E_y^2 + E_z^2) \quad dV, \quad (7)$$

the plasma electric field energy. The total energy remains nearly constant throughout the duration of the simulation. The small amount of numerical cooling we observe is a characteristic of non-energy-conserving semi-implicit discretizations, which tend to remove energy from the system, while explicit discretizations tend to introduce numerical heating. An energy-conserving semi-implicit discretization has recently been introduced in G. Lapenta (2017) but has not been used in the present work. We remark that the physical significance of the simulation is ensured by the fact that the amount of energy converted at the end of linear phase ($\approx 0.05\%$ at the peak) is well above the amount of numerical cooling both at the same time ($\approx 0.005\%$ at $t = 72\omega_p^{-1}$) and also at the end of the simulation ($\approx 0.015\%$ at $t = 300\omega_p^{-1}$).
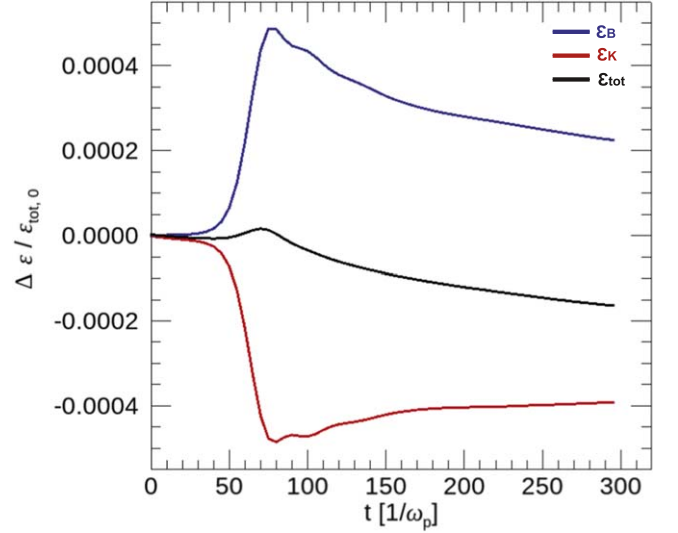

Figure 2. Temporal evolution of the normalized variation of magnetic energy (blue), kinetic energy (red), and total energy (black).

3.1. Temporal Evolution of the Electron VDF

To study how electromagnetic fluctuations affect the plasma, in Figure 3 we plot the electron distribution function $f_e(v_\parallel, v_{\perp 1}, v_{\perp 2})$ at the beginning of the simulation and at the end of the linear growth phase of the instability. Figure 3(a) shows a 3D view of the initial electron VDF shown in Figure 1(b) in a 2D plane. We see the presence of a dense, isotropic core and the high-energy features characteristic of electron VDFs in the solar wind: the dynamic deficit−strahl −halo system. In Figure 3(b), we show how the electron VDF is modified after the generation of the instability. In particular, the interaction between the electrons and the generated waves results in the filling of the electron deficit and leads to an electron distribution that is quasi-isotropic during the saturation phase of the instability. The animation of Figure 1 illustrates the temporal evolution of the electron VDF over the duration of the simulation. It starts at the beginning of the simulation, progresses through the onset of wave generation, and continues to the saturation phase. The interaction with the generated waves is shown to fill the electron deficit and isotropize the distribution. An electron distribution with a deficit, in the presence of suprathermal electrons (some of them with a negative parallel velocity component as a consequence of previous scattering), leads to an electromagnetic instability. The fluctuations generated by the instability result in wave−particle interactions such that the deficit is gradually filled. Protons are not shown because they are initialized in an equilibrium situation and remain largely unperturbed throughout the duration of the simulation.
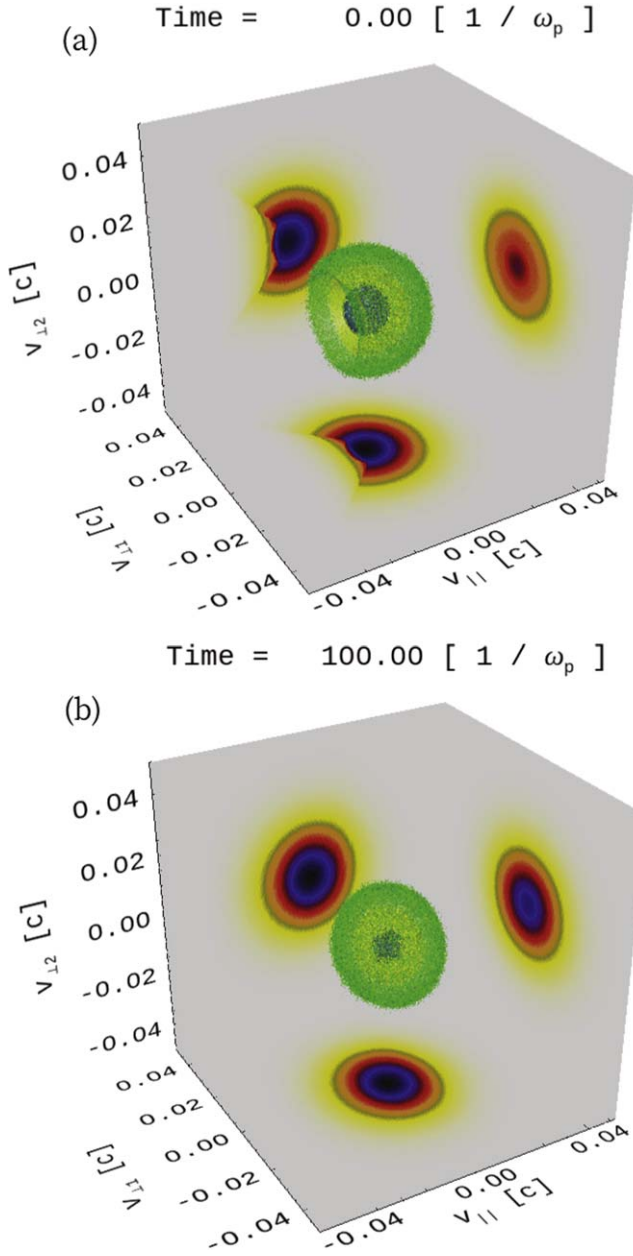
(a)   Time =   0.00 [1 / ω_p]

(b)

Time =   100.00 [1 / ω_p]

Figure 3. Electron VDF $f_e = f(v_\parallel, v_{\perp 1}, v_{\perp 2})$ at (a) $t_0 = 0$ and (b) $t = 100\omega_p^{-1}$. An animated version of this figure is available. It dynamically illustrates the evolution of the electron VDF throughout the simulation. The animation runs from $t_0 = 0$ to $100\omega_p^{-1}$. The real-time duration of the animation is 5.4 s.

(An animation of this figure is available in the online article.)

We show in Figure 4 the difference between the electron VDF near the peak of the instability ($f_e(t = 80\omega_p^{-1})$) and at time zero, to understand which electrons are scattered into the vacant sunward region. The electrons affected by scattering processes with the waves generated during the instability occupy a specific region of phase space: electrons adjacent to the deficit, due to wave−particle resonance interactions, are scattered into a region of phase space that was not initially populated by electrons.

3.2. Nature of the Electromagnetic Waves

We now investigate in detail the nature of the instability we observe and the electromagnetic waves it produces. Figure 5(a)
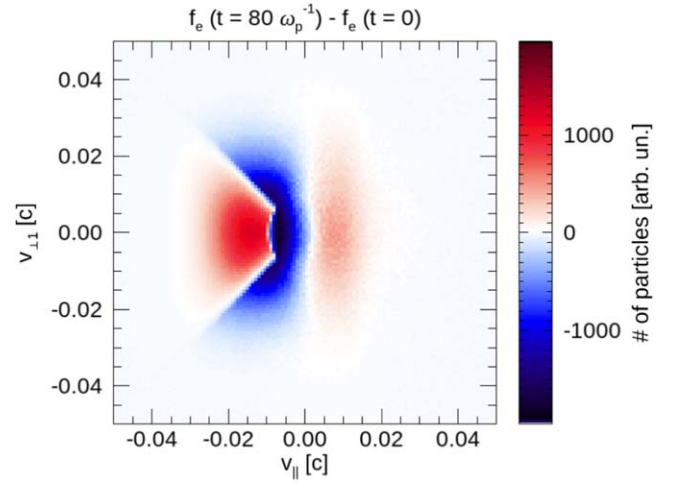
$f_e (t = 80 \, \omega_p^{-1}) - f_e (t = 0)$

Figure 4. Difference between the electron velocity distribution function near the peak of the instability and that at time zero ($f_e(t = 80\omega_p^{-1}) - f_e(t = 0)$).
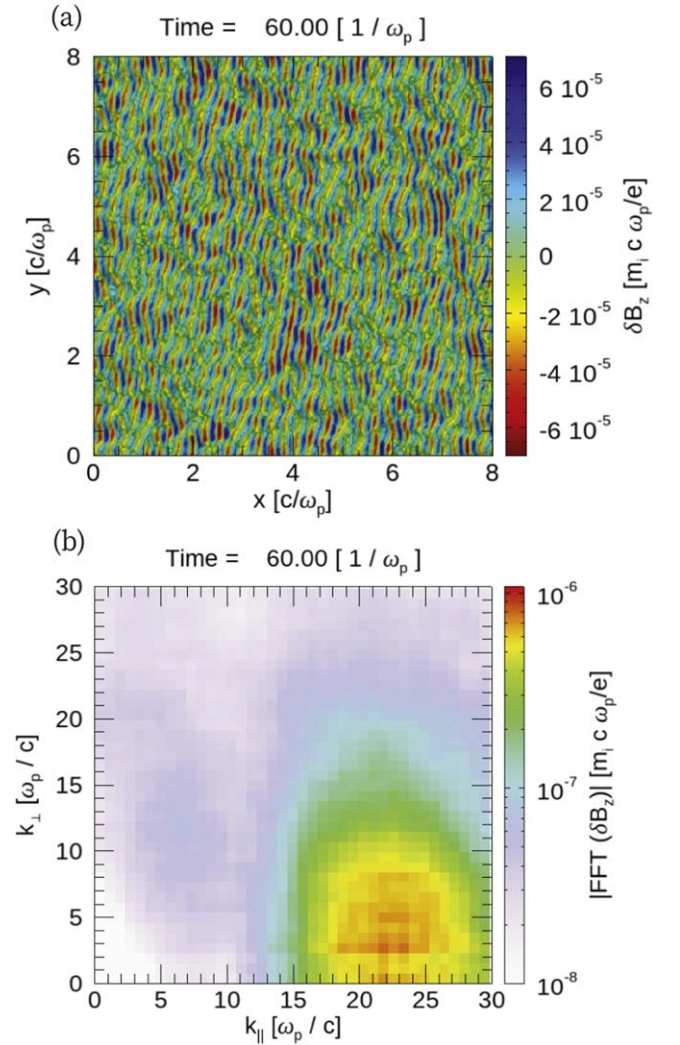
(a)   Time =   60.00 [1 / ω_p]

(b)   Time =   60.00 [1 / ω_p]

Figure 5. Out-of-plane magnetic field fluctuations during (a) the instability growing phase ($\delta B_z(t = 60\omega_p^{-1})$) and (b) its FFT. An animated version of panel (a) in this figure is available. It dynamically shows the temporal evolution of $\delta B_z(t)$ in the x–y plane during the simulation. The animation runs from $t = 0$ to $295\omega_p^{-1}$. The real-time duration of the animation is 4.4 s.

(An animation of this figure is available in the online article.)

shows the transverse magnetic fluctuations in the $x-y$ plane during the growing phase of the instability at $t = 60\omega_p^{-1}$. The fluctuations are calculated as $\delta B_z(t) = B_z(t) - B_0$. The waves have a direction of propagation that is mainly parallel to $\boldsymbol{B}_0 = B_0\hat{e}_x$, and the box is large enough to contain multiple oscillations of the fastest-growing waves. The animation illustrates the temporal evolution of $\boldsymbol{\delta B_z(t)}$ in the $\boldsymbol{x-y}$ plane throughout the simulation. It begins at $\boldsymbol{t = 0}$, progresses through the growing phase of the instability, and shows the development and propagation of wave crests moving from left to right of the spatial domain. Figure 5(b) shows the power spectrum of the out-of-plane magnetic field fluctuations, obtained with a fast Fourier transform (FFT) FFT($\delta B_z(t)$), in the $k_\parallel - k_\perp$ plane, where $k_\parallel$ and $k_\perp$ are the wavevectors parallel and perpendicular to B_0, with $k = 2\pi/\lambda$, where λ is the wavelength. The instability leads to the generation of unstable electromagnetic waves propagating in a quasi-parallel direction to the background magnetic field. In particular, the fastest-growing modes are concentrated between $20\,d_p^{-1} < k_\parallel < 26\,d_p^{-1}$ and $0 < k_\perp < 6\,d_p^{-1}$, with an angle of propagation of most unstable waves ranging from zero up to $20°$ with respect to the background magnetic field. The simulation box we have chosen is capable of containing more than 25 oscillations of the fastest-growing mode, considering it to be characterized by a wavelength $\lambda = 2\pi/(20\,d_p^{-1})$. The waves migrate to progressively lower $k_\parallel$ as the deficit is filled (not shown in this paper).

Figure 6(a) shows the spacetime Fourier power spectrum, i.e., the frequency with which the waves propagate as a function of the wavevector $k_\parallel$. We first note that most waves propagate away from the Sun, i.e., in the positive, antisunward direction. This is in line with what has been described above regarding the time evolution of the electron VDF: the electrons that resonate with the waves generated during the instability are those that move in the opposite direction to the waves, and they are scattered and go to fill the sunward deficit. From Figure 6(a), we observe that the waves propagate at a frequency between $0.025\omega_p^{-1}$ and $0.13\omega_p^{-1}$. Our electron gyrofrequency ($\Omega_e = eB_0/(m_ec)$) normalized to the proton (electron) plasma frequency is $\Omega_e/\omega_p = 0.42$ ($\boldsymbol{\Omega_e/\omega_e} = 0.01$); hence, the range of frequencies at which most waves propagate fulfills $0.06\Omega_e \leqslant \omega_r \leqslant 0.3\Omega_e$. The frequencies at which the waves propagate are characteristic of fast-magnetosonic/whistler waves ($\omega_r < \Omega_e$; e.g., D. Stansby et al. 2016). The cyclotron resonance condition for parallel-propagating whistler waves (D. Verscharen et al. 2019a) is given by

$$\omega_r - \Omega_e = k_\parallel v_\parallel. \tag{8}$$

Since $\omega_r < \Omega_e$ for whistler waves, Equation (8) demands that the resonance interaction only occurs when $k_\parallel v_\parallel < 0$. This means that parallel whistler waves only scatter electrons that travel in the opposite direction to the waves; in this case, we have positively (antisunward) propagating waves that scatter electrons with negative (sunward) parallel velocity.

Figure 6(b) depicts the wave hodogram, obtained by plotting B_y versus B_z at the center of the domain $x = y = 4d_p$ as a function of time, starting from the end of the quasi-stationary phase ($t^* = 50\omega_p^{-1}$) to the end of the simulation ($t_{\mathrm{end}} = 300\omega_p^{-1}$). We observe that the wave is almost circularly and purely right-hand polarized (the x-axis points out of the page), which is again consistent with our interpretation of these waves as parallel-propagating whistler waves.
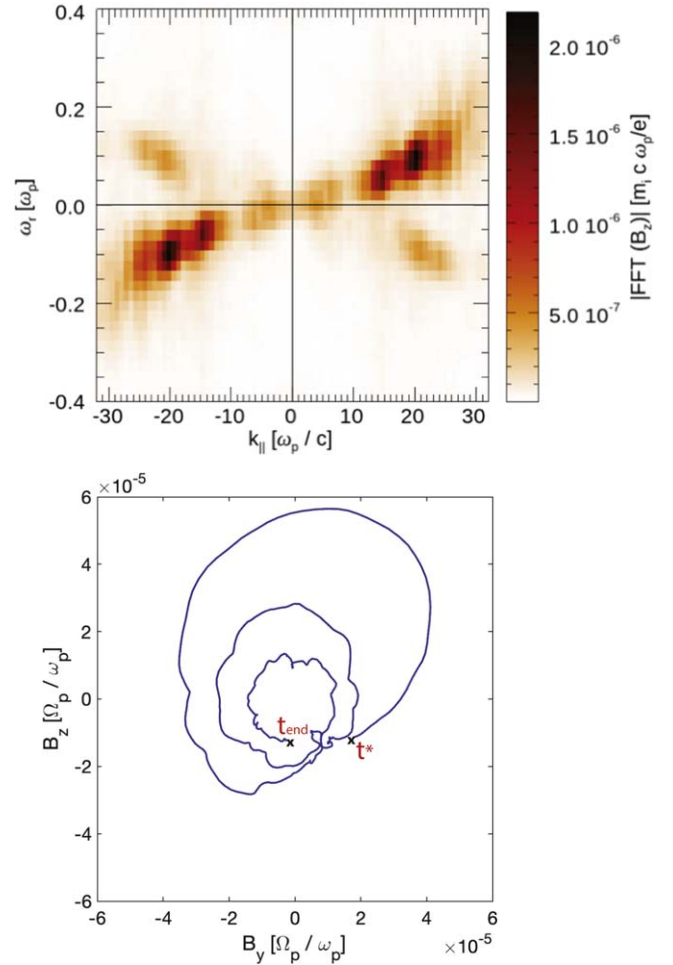

Figure 6. (a) Spacetime Fourier power spectrum $k_\parallel - \omega_r$ of predominately antisunward whistler waves propagating along the background magnetic field direction. (b) Hodogram of right-hand-polarized whistler waves. B_x is directed out of the page.

We therefore conclude that a distribution function that is in line with those commonly observed in the heliosphere near the Sun, where an electron deficit is commonly present, leads to the generation of quasi-parallel, right-hand circularly polarized waves that propagate away from the Sun with frequencies $\omega_r < \Omega_e$. We identify these waves as antisunward-propagating whistler waves.

4. Discussion and Conclusions

We explore via a fully kinetic simulation a possible scenario for the erasure of the sunward electron deficit. While already predicted by exospheric models (e.g., J. Lemaire & M. Scherer 1973; M. Maksimovic et al. 1997), systematic observations of the electron deficit have been made possible only by the recent PSP and SO campaigns (e.g., L. Berčič et al. 2021b; J. S. Halekas et al. 2021a).

In our simulation, unstable quasi-parallel antisunward whistler waves are generated by the departure from the thermal equilibrium of the electron VDF owing to the presence of the deficit itself. The waves we observe, as characteristic for whistler waves, have a frequency $\omega_r < \Omega_e$, and since they propagate along the direction of the magnetic field, they exhibit right-hand circular polarization. We show that the simulated

whistler instability resonantly scatters electrons from neighboring regions in phase space into the deficit, effectively erasing it.

This work proposes a possible mechanism that leads to the generation of quasi-parallel whistler waves in the solar wind. These waves propagate away from the Sun with a frequency of the order of $0.1 \approx \Omega_e$. This is of high importance in the recent observational context, as most of the wave parameters are in accordance with what PSP and SO measured during their near-Sun data acquisition. Various observational studies prove that a very high percentage of the whistler waves measured in the young solar wind propagate in a quasi-parallel direction to the magnetic field (e.g., V. K. Jagarlamudi et al. 2021; C. Froment et al. 2023; K.-E. Choi et al. 2024) and that a large proportion of them propagate in the antisunward direction (M. Kretzschmar et al. 2021; L. Colomban et al. 2024). L. Berčič et al. (2021b), analyzing SO data, find a direct correlation between the detection of whistler waves and the presence of the deficit in the electron VDF. Notably, the waves observed by L. Berčič et al. (2021b) are also predominantly quasi-parallel and propagate away from the Sun. The waves generated during the instability proposed and studied in this work have proprieties matching those of the recent observational studies (e.g., C. Froment et al. 2023; K.-E. Choi et al. 2024; L. Colomban et al. 2024) but also those of many other less recent observations (e.g., C. Lacombe et al. 2014; D. Stansby et al. 2016; Y. Tong et al. 2019).

We also show how the whistler waves, propagating away from the Sun, resonate predominantly with sunward electrons (traveling in the opposite direction to the waves). This ensures that these waves do not interact with the electron strahl. However, wave−particle interactions lead to the filling of the deficit. As the initial deviation from thermodynamic equilibrium is reduced, a decrease in the electron heat flux (defined as the third moment of the VDF) occurs. According to J. S. Halekas et al. (2021b), while the drifting electron core represents the sunward contribution of heat flux in the solar wind, the deficit and strahl represent the generally larger antisunward contribution. Hence, although antisunward parallel whistler waves do not interact with the strahl, they are able to suppress part of the heat flux that the solar wind carries. The instability described in this paper adds to the possible noncollisional mechanisms responsible for heat flux regulation, as also described by J. T. Coburn et al. (2024) in their analysis of SO measurements. This is especially valid in the slow solar wind, where the nonthermality of the electron distribution function is not predominantly related to the presence of the strahl as it is in the fast solar wind (E. Marsch et al. 2004).

We describe a possible scenario that correlates the different suprathermal species characteristics of the electron VDF, i.e., strahl, halo, and deficit, with parallel and oblique whistler waves. We envision a multistep process that can be broken into the following stages:

1. The strahl generates sunward-directed oblique and parallel whistler waves owing to the whistler heat flux instability.
2. Sunward-directed whistler waves scatter the strahl into the halo. During this process, the oblique whistler waves shift toward smaller propagation angles until they become quasi-aligned with the ambient magnetic field. This mechanism of quasi-parallel sunward whistler wave generation is described in detail in A. Micera et al. (2020b, 2021).

3. Antisunward quasi-parallel whistler waves are triggered by the interplay of strahl and halo with a further feature of the electron VDF, the deficit. While the strahl population is scattering in the halo, there is a resulting configuration, reproduced here, composed of strahl−halo−deficit that leads to the instability analyzed in this paper.
4. The deficit is filled as a result of the resonant interaction between the electrons adjacent to it and the antisunward quasi-parallel whistler waves generated by the instability.

We have thus provided an overall picture of the types of processes that can produce the range of whistler waves observed in the solar wind, without having to call into question the whistler anisotropy instability (I. Y. Vasko et al. 2019) or the electron fire hose instability. The whistler anisotropy instability is an unlikely candidate for whistler wave production in the solar wind because it requires values of $T_{e,\perp} > T_{e,\parallel}$ to be triggered (rarely measured in conjunction with the observation of whistler waves; e.g., D. Stansby et al. 2016). The electron fire hose instability, instead, generates low-frequency left-hand polarized waves (A. Micera et al. 2020a) or nonpropagating waves ($\omega_r = 0$; E. Camporeale & D. Burgess 2008; R. A. López et al. 2022).

In validating and comparing our findings against current observations, three recent studies are noteworthy. C. Cattell et al. (2022) discuss the lack of clear evidence of whistler waves when the PSP samples the solar wind inside approximately $25R_s$. J. S. Halekas et al. (2021a) show that while the deficit is an almost ubiquitous feature of the pristine solar wind in which the PSP is immersed, the clear evidence of this feature fades as the spacecraft moves farther from the Sun.

K.-E. Choi et al. (2024) observe that most of the whistler waves in the young solar wind between $25R_s$ and $40R_s$ propagate toward the Sun, while an increasing occurrence of antisunward-propagating whistler waves is observed between $40R_s$ and $55R_s$. Furthermore, consistent with C. Cattell et al. (2022), a sharp decrease in the occurrence of whistler waves is noted around $25R_s$.

These observations can be explained as follows: In the inner heliosphere, the electric potential is large; hence, the deficit is commonly present. The suprathermal population consists mostly of the strahl, as the relative density of the halo near the Sun is negligible (J. S. Halekas et al. 2020). The strahl is not yet unstable, due to the low value of its drift velocity compared to the Alfvén velocity (R. A. López et al. 2020; A. Micera et al. 2021). Hence, the production of whistler waves by the strahl is suppressed.

Additionally, no "scattered electrons" are present in the phase-space region characterized by $v_\parallel < 0$. In this configuration, all whistler waves interacting with the deficit at $v_\parallel < 0$ undergo damping and are therefore not observable. It is only in the presence of scattered electrons with $v_\parallel < 0$ that whistler waves can grow and become detectable. Thus, in regions where only the "core" component exists and no "scattered electrons" are present at $v_\parallel < 0$, antisunward parallel whistler waves are significantly damped owing to cyclotron resonance with core electrons.

This provides an explanation for the diminishing whistler wave activity closer to the Sun, consistent with the observations reported in C. Cattell et al. (2022) and K.-E. Choi et al. (2024).

As the distance from the Sun increases, the Alfvén velocity decreases, making the strahl unstable to the oblique whistler

heat flux instability (D. Verscharen et al. 2019a; A. Micera et al. 2021). This instability leads to the generation of predominantly sunward-propagating whistler waves. Farther away from the Sun, the scattering processes between the strahl and sunward whistler waves become more significant, resulting in electron distribution functions similar to those simulated in this study. These distributions can be considered a primary source of antisunward whistler waves. This entire process leads to an increase in the relative density of the halo at the expense of the strahl and to the filling of the deficit as the heliocentric distance increases, in agreement with J. S. Halekas et al. (2021a).

The linear analysis of this new instability would help to understand the physics of the shown instability more clearly. Due to the very non-Maxwellian shape of the distribution, classical solvers to the linear Vlasov–Maxwell dispersion relation cannot evaluate the linear stability of this system. The code ALPS (D. Verscharen et al. 2018), which specifically addresses the stability of the system characterized by non-Maxwellian distribution functions, will be used for a follow-up analysis.

To conclude, this work aims at addressing one of the most fascinating topics in heliospheric physics: the link between global and kinetic scales. The electron deficit is a consequence of global electron circulation patterns, while the instability that erases it is a microscope kinetic instability linked to the process of strahl-to-halo scattering, which is in turn associated with a process of global significance such as heat flux regulation in the heliosphere (D. Verscharen et al. 2019b).

ORCID iDs

Alfredo Micera ◉ https://orcid.org/0000-0001-9293-174X
Daniel Verscharen ◉ https://orcid.org/0000-0002-0497-1096
Jesse T. Coburn ◉ https://orcid.org/0000-0002-2576-0992
Maria Elena Innocenti ◉ https://orcid.org/0000-0002-5782-0013

References

Berčič, L., Larson, D., Whittlesey, P., et al. 2020, ApJ, 892, 88
Berčič, L., Maksimović, M., Halekas, J. S., et al. 2021a, ApJ, 921, 83
Berčič, L., Verscharenć, D., Owen, C. J., et al. 2021b, A&A, 656, A31
Boldyrev, S., Forest, C., & Egedal, J. 2020, PNAS, 117, 9232
Camporeale, E., & Burgess, D. 2008, JGRA, 113, A07107
Cattell, C., Breneman, A., Dombeck, J., et al. 2021, ApJL, 911, L29
Cattell, C., Breneman, A., Dombeck, J., et al. 2022, ApJL, 924, L33
Choi, K.-E., Agapitov, O., Colomban, L., et al. 2024, ApJ, 971, 177
Coburn, J. T., Verscharen, D., Owen, C. J., et al. 2024, ApJ, 964, 100
Colomban, L., Kretzschmar, M., Krasnoselkikh, V., et al. 2024, A&A, 684, A143
Feldman, W. C., Asbridge, J. R., Bame, S. J., Montgomery, M. D., & Gary, S. P. 1975, JGR, 80, 4181
Fox, N. J., Velli, M. C., Bale, S. D., et al. 2016, SSRv, 204, 7
Froment, C., Agapitov, O. V., Krasnoselskikh, V., et al. 2023, A&A, 672, A135
Halekas, J. S., Berčič, L., Whittlesey, P., et al. 2021a, ApJ, 916, 16
Halekas, J. S., Whittlesey, P., Larson, D. E., et al. 2020, ApJS, 246, 22
Halekas, J. S., Whittlesey, P. L., Larson, D. E., et al. 2021b, A&A, 650, A15
Hockney, R. W., & Eastwood, J. W. 1988, Computer Simulation Using Particles (Bristol: Hilger)
Innocenti, M. E., Boella, E., Tenerani, A., & Velli, M. 2020, ApJL, 898, L41
Innocenti, M. E., Johnson, A., Markidis, S., et al. 2017, Adv. Eng. Software, 111, 3
Innocenti, M. E., Tenerani, A., Boella, E., & Velli, M. 2019, ApJ, 883, 146
Jagarlamudi, V. K., Dudok de Wit, T., Froment, C., et al. 2021, A&A, 650, A9
Jeong, S.-Y., Verscharen, D., Wicks, R. T., & Fazakerley, A. N. 2020, ApJ, 902, 128
Jockers, K. 1970, A&A, 6, 219
Komarov, S., Schekochihin, A. A., Churazov, E., & Spitkovsky, A. 2018, JPlPh, 84, 905840305
Kretzschmar, M., Chust, T., Krasnoselskikh, T., et al. 2021, A&A, 656, A24
Lacombe, C., Alexandrova, O., Matteini, L., et al. 2014, ApJ, 796, 5
Landi, S., & Pantellini, F. 2003, A&A, 400, 769
Lapenta, G. 2017, JCoPh, 334, 349
Lapenta, G., Brackbill, J. U., & Ricci, P. 2006, PhPl, 13, 055904
Lemaire, J., & Scherer, M. 1971, JGR, 76, 7479
Lemaire, J., & Scherer, M. 1973, RvGSP, 11, 427
Lie-Svendsen, Ø., Hansteen, V. H., & Leer, E. 1997, JGRA, 102, 4701
López, R. A., Lazar, M., Shaaban, S. M., Poedts, S., & Moya, P. S. 2020, ApJL, 900, L25
López, R. A., Micera, A., Lazar, M., et al. 2022, ApJ, 930, 158
Maksimovic, M., Pierrard, V., & Lemaire, J. 2001, Ap&SS, 277, 181
Maksimovic, M., Pierrard, V., & Lemaire, J. F. 1997, A&A, 324, 725
Maksimovic, M., Zouganelis, I., Chaufray, J. Y., et al. 2005, JGRA, 110, A09104
Markidis, S., Lapenta, G., & Rizwan-uddin 2010, Math. Comput. Simul., 80, 1509
Marsch, E., Ao, X. Z., & Tu, C. Y. 2004, JGRA, 109, A04102
Meyer-Vernet, N. 2007, Basics of the Solar Wind (Cambridge: Cambridge Univ. Press)
Meyer-Vernet, N., & Issautier, K. 1998, JGRA, 103, 29705
Micera, A., Boella, E., Zhukov, A. N., et al. 2020a, ApJ, 893, 130
Micera, A., Zhukov, A. N., López, R. A., et al. 2020b, ApJL, 903, L23
Micera, A., Zhukov, A. N., López, R. A., et al. 2021, ApJ, 919, 42
Müller, D., Marsden, R. G., St. Cyr, O. C., & Gilbert, H. R. 2013, SoPh, 285, 25
Pierrard, V., & Lemaire, J. 1996, JGR, 101, 7923
Pierrard, V., Maksimovic, M., & Lemaire, J. 1999, JGRA, 104, 17021
Pilipp, W. G., Miggenrieder, H., Montgomery, M. D., et al. 1987, JGR, 92, 1075
Roberg-Clark, G. T., Agapitov, O., Drake, J. F., & Swisdak, M. 2019, ApJ, 887, 190
Rosenbauer, H., Schwenn, R., Marsch, E., et al. 1977, JGZG, 42, 561
Scime, E. E., Bame, S. J., Feldman, W. C., et al. 1994, JGR, 99, 23401
Scudder, J. D. 1996, JGRA, 101, 13461
Stansby, D., Horbury, T. S., Chen, C. H. K., & Matteini, L. 2016, ApJL, 829, L16
Stverák, V., Maksimovic, M., Trávníček, P. M., et al. 2009, JGRA, 114, A05104
Tang, B., Zank, G. P., & Kolobov, V. I. 2020, ApJ, 892, 95
Tong, Y., Vasko, I. Y., Pulupa, M., et al. 2019, ApJL, 870, L6
Vasko, I. Y., Krasnoselskikh, V., Tong, Y., et al. 2019, ApJL, 871, L29
Verscharen, D., Chandran, B. D. G., Jeong, S.-Y., et al. 2019a, ApJ, 886, 136
Verscharen, D., Klein, K. G., Chandran, B. D. G., et al. 2018, JPlPh, 84, 905840403
Verscharen, D., Klein, K. G., & Maruca, B. A. 2019b, LRSP, 16, 5
Vocks, C., Salem, C., Lin, R. P., & Mann, G. 2005, ApJ, 627, 540
Zouganelis, I., Meyer-Vernet, N., Landi, S., Maksimovic, M., & Pantellini, F. 2005, ApJL, 626, L117